

Probabilistic Local Features in Uncertain Vector Fields with Spatial Correlation

Christoph Petz, Kai Pöthkow and Hans-Christian Hege

Zuse Institute Berlin (ZIB), Berlin, Germany

Abstract

In this paper methods for extraction of local features in crisp vector fields are extended to uncertain fields. While in a crisp field local features are either present or absent at some location, in an uncertain field they are present with some probability. We model sampled uncertain vector fields by discrete Gaussian random fields with empirically estimated spatial correlations. The variability of the random fields in a spatial neighborhood is characterized by marginal distributions. Probabilities for the presence of local features are formulated in terms of low-dimensional integrals over such marginal distributions. Specifically, we define probabilistic equivalents for critical points and vortex cores. The probabilities are computed by Monte Carlo integration. For identification of critical points and cores of swirling motion we employ the Poincaré index and the criterion by Sujudi and Haimes. In contrast to previous global methods we take a local perspective and directly extract features in divergence-free fields as well. The method is able to detect saddle points in a straight forward way and works on various grid types. It is demonstrated by applying it to simulated unsteady flows of biofluid and climate dynamics.

Categories and Subject Descriptors (according to ACM CCS): I.3.3 [Computer Graphics]: Picture/Image Generation—Viewing algorithms I.6.8 [Simulation and Modeling]: Types of Simulation—Monte Carlo, Visual G.3 [Mathematics of Computing]: Probability and Statistics—Probabilistic algorithms

1. Introduction

Scientific data obtained by measurements or numerical simulations is always affected by uncertainty due to limited measurement accuracy, lack of control of parameters, model uncertainty, discretization or quantization errors. Furthermore, there are aleatoric phenomena that are intrinsically random. Feynman *et al.* therefore stated in their famous textbook [FLS63]: “Our most *precise* description of nature must be in terms of *probabilities*”. Modeling, simulation and visualization techniques thus should take care of uncertainties.

In previous work several approaches to visualize uncertain vector fields have been proposed. However, these methods assume the vectors of the field to be statistically independent, i.e. they only consider pointwise marginal distributions but no spatial correlations. The correlation structure, however, is an essential property of random fields and it has been shown that it has significant impact on feature extraction methods by Pöthkow *et al.* [PWH11] and Pfaffelmoser *et al.* [PRW11]. Taking the correlations into account increases

the dimensionality of the data compared to independent distributions. Direct visualization (using e.g. glyphs) is therefore very challenging or not feasible at all.

We propose methods to compute spatial distributions of local features from uncertain vector fields considering the local correlation structure. These distributions can be used to display important structures of the data. For the current work we focus on critical points (sources, sinks and saddles) and swirling motion vortex cores, but the proposed general approach can be applied to other local features as well.

Our model and the computational framework extends that of Pöthkow *et al.* [PWH11] for discretized random scalar fields to vector fields being sampled on cells or nodes of structured or unstructured grids. The resulting probabilities for the presence of a feature at spatial locations are computed using a Monte Carlo method.

In this framework it is assumed that the random variables are Gaussian distributed. Of course, not all uncertain vector fields are normally distributed, but for many of them this

is approximately the case for fundamental reasons (central limit theorem). Whether or not a given field is Gaussian, can either be statistically tested or assured by empirical knowledge and statistical considerations. An example of the second case are measurements of blood flow and tissue velocity by phase contrast MRI; due to the inherent noise in MRI the resulting vector fields are uncertain and can be shown to be correlated Gaussian random fields [FHH^{*}10].

An interesting question from the application point of view is the locality of features, i.e. the question how far regions, in which some feature is notably present, are extended.

The major contributions of the paper are

- the definition of a mathematical model for uncertain vector fields considering spatial correlation,
- a general framework for probabilistic extraction of local features from uncertain vector fields,
- specific methods for probabilistic extraction of critical points and (swirling motion) vortex cores, and the
- application of these methods to data from biofluid mechanics and climate research, with results, e.g., concerning the spatial locality of features.

2. Related Work

An introduction to uncertainty visualization describing various aspects of uncertainty propagation and several visualization methods was presented by Pang *et al.* [PWL97]. Johnson and Sanderson [JS03] considered the representation of uncertainty to be a major challenge in visualization research.

Visualizations of uncertain vector fields can be created using specific texture mapping approaches as proposed by Botchen *et al.* [BWE05]. Hlawatsch *et al.* [HLNW11] introduced glyphs for the static visualization of unsteady flow with uncertainty indicated by angular confidence intervals. Allendes Osorio and Brodlie [AOB09] adapted LIC (Line Integral Convolution) visualization methods to indicate directional uncertainties in vector fields. Specific visualization techniques for uncertain flow fields include uncertainty glyphs [WPL96], stream ribbons and envelopes showing streamline uncertainty [LPSW96] and the incorporation of uncertainty in reaction-diffusion visualizations [SJK04]. The uncertainty of particle positions and movements was estimated and visualized by Lodha *et al.* [LFC02]. Zuk *et al.* [ZDG^{*}08] used glyphs and an interactive tool to visualize and explore uncertain bidirectional vector fields. Bhatia *et al.* [BJB^{*}11] visualized uncertainty introduced by streamline computation of crisp vector fields. Szymczak [Szy11] proposed methods to compute Morse decompositions given a user-specified error bound and with respect to perturbation of the piecewise constant input vector field.

A global approach to feature extraction is uncertain vector field topology, as presented by Otto *et al.* [OGHT10]. Subsequent work extended these methods to detect closed streamlines [OGT11a] and topological structures of 3D vector fields [OGT11b]. However, none of these approaches

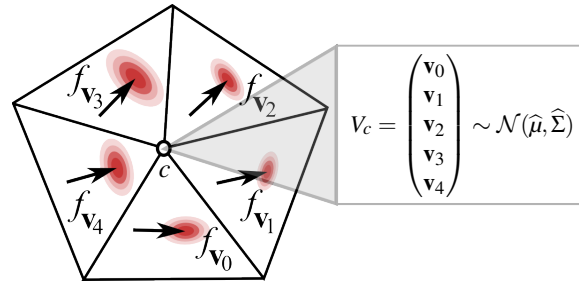


Figure 1: Illustration for the star of a vertex c in a triangulated domain with uncertain vectors defined per triangle. The marginal PDFs are indicated for each vector. The local correlated random vector V_c consists of all vector components of the neighborhood of c .

considered spatial correlations in the respective uncertainty model. Our mathematical model is an extension of the models for uncertain scalar fields described in the work by Pöthkow *et al.* [PH11, PWH11]. An alternative model with exponential correlation functions was presented in [PRW11]. For the current work we extend the model of [PWH11] to vector fields sampled on structured or unstructured grids, representing them as multidimensional Gaussian random fields.

Various local features of crisp vector fields as well as methods for extraction have been proposed. Particularly for flow fields there exists a large body of work, see e.g. [HH89, PVH^{*}03, LHZP07, MLP^{*}10]. A specific indicator of critical points in 2D and 3D vector fields is the Poincaré-Hopf index [GTS04, TG09]. Polthier and Preuß presented operators to classify vector field singularities in piecewise constant vector fields [PP02]. Centers of locally swirling flow can be detected using the approach presented by Sujudi and Haimes [SH95].

3. Probabilistic Model for Uncertain Vector Fields

As input we consider uncertain N -dimensional vector fields discretized on a computational grid with M sample points. The uncertainties are modeled by considering all vector components as random variables. The components of all vectors can be represented as a single random vector V , for example

$$V = (v_0, v_1, \dots, v_{M-1})^T = (x_0, y_0, z_0, x_1, \dots)^T,$$

for $N = 3$. We assume that V conforms to a multidimensional Gaussian distribution that is characterized by a probability density function f with means $\mu \in \mathbb{R}^{MN}$ and covariance matrix $\Sigma \in \mathbb{R}^{(MN) \times (MN)}$. Note that both covariances between vector components of each vector v_i and covariances between components of all pairs of vectors (v_i, v_j) are considered.

Data values might be defined on any grid entity like nodes, edges, faces or volume cells. We use the notion of η -cell, where η denotes the dimensionality of the cell, e.g., 0 for nodes and 1 for edges. We denote the set of all η -cells of a grid by C_η . The full covariance matrix in this setting grows quadratically with the number of sample points M . In this paper, we consider local features that can be identified by operators acting locally on data values in the neighborhood of an η -cell $c \in C_\eta$. The size of the neighborhood depends on the feature definition and data location. Fig. 1 depicts the neighborhood of a 0-cell (node) of an uncertain vector field defined on the faces of a triangulated domain (2-cells). Let K_c be the number of degrees of freedom in the neighborhood of c , then only marginal distributions of K_c random variables are considered, and the covariance function reduces to

$$\hat{\Sigma} : C_\eta \rightarrow \mathbb{R}^{K_c N \times K_c N}. \quad (1)$$

The total size of the marginalized covariance matrices is linear with the number of cells. Similarly, mean values can be condensed to cell neighborhoods, yielding

$$\hat{\mu} : C_\eta \rightarrow \mathbb{R}^{K_c N}. \quad (2)$$

The correlated random vector V_c for each η -cell c and the neighborhood of c is defined by a multidimensional normal PDF f_c that is described by $\hat{\mu}$ and $\hat{\Sigma}$. It is a specific property of Gaussian fields the $\hat{\Sigma}$ and $\hat{\mu}$ are independent of mean values and covariances that correspond to cells outside the neighborhood. Thus, the local marginal distribution f_c can be trivially determined for Gaussian fields only, see e.g. [PWH11].

4. Probabilistic Feature Extraction

In the following, we formulate a generic algorithm for computing cell-wise probabilities for the occurrence of locally defined features. Afterwards, we apply this to critical point and vortex core extraction in vector fields.

A *feature indicator* I is a boolean function defined for an η -cell c and a realization of V_c that determines if a feature occurs or not:

$$I : C_\eta \times \mathbb{R}^{K_c N} \rightarrow \{0, 1\} \quad (3)$$

Note that the neighborhood size of a cell is in general not the same for every cell in the grid, and depends on the combinatorial grid topology.

Let I be a feature indicator defined on η -cells of a computational grid with corresponding $\hat{\mu}$ and $\hat{\Sigma}$. The cell-wise probability for the occurrence of the feature is then

$$P(c) = \int_D f_c(\mathbf{v}) d\mathbf{v} = \int_{\mathbb{R}^{K_c N}} f_c(\mathbf{v}) I(c, \mathbf{v}) d\mathbf{v} = E(I(c, \cdot)), \quad (4)$$

where $D = \{\mathbf{v} \in \mathbb{R}^{K_c N} | I(c, \mathbf{v}) = 1\}$ and f_c is probability density function of the multivariate Gaussian distribution specified by $\hat{\mu}$ and $\hat{\Sigma}$. The probability $P(c)$ can also be considered as the expected value of the feature indicator in cell c .

4.1. Vector Field Critical Points

Isolated critical points in a crisp vector field $\mathbf{v}(x)$ are the points of the domain where the vector field is 0, e.g., the set of x with $\mathbf{v}(x) = 0$, and the vector field is non-zero in an infinitesimal small neighborhood of those points.

The Poincaré index relates the occurrence of critical points in a volume to the vectors on the surface of that volume. It measures the signed winding number of the vectors along the surface of an oriented topological sphere. If the index is non-zero, the sphere encloses an isolated critical point. The sign of the Poincaré index is the same as the sign of the determinant of the Jacobian matrix of the vector field at the critical point.

4.1.1. Critical Points in 2D

In 2D, the vectors along a path are traversed in counter-clockwise direction as illustrated in Fig. 2, vector directions along the path cover a circle an integer multiple of times.

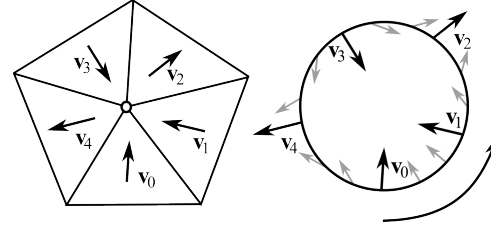


Figure 2: Winding number calculation of a saddle point in a piecewise constant triangulated vector field. Following vectors in counter-clockwise direction from v_0 to v_4 , vectors rotate clockwise, yielding the winding number of -1 .

We use the Poincaré index for the identification of critical points by considering the vectors on the surface of the neighborhood. We compute discrete angles between adjacent vectors in $[-\pi, \pi]$, i.e., the smaller angle of the two possible rotation directions. This is equivalent to component-wise linear interpolation of vectors, and can be seen as follows: consider two linearly interpolated vectors \mathbf{v}_0 and \mathbf{v}_1 ,

$$\mathbf{v}(t) = (1-t)\mathbf{v}_0 + t\mathbf{v}_1, \quad (5)$$

with $t \in [0, 1]$. The vector product $\mathbf{v}_0 \times \mathbf{v}(t)$ is

$$\mathbf{v}_0 \times \mathbf{v}(t) = (1-t)\mathbf{v}_0 \times \mathbf{v}_0 + t\mathbf{v}_0 \times \mathbf{v}_1 = t\mathbf{v}_0 \times \mathbf{v}_1. \quad (6)$$

Thus, for $t \in (0, 1]$, rotation angles are in the same direction as the smaller angle between \mathbf{v}_0 and \mathbf{v}_1 , i.e., the angular range covered by two linearly interpolated vectors is the same as the angle between the start- and end vector of the interpolation.

Piecewise Constant Fields. For piecewise constant tangent vector fields of a curved triangulated domain, we compute the Poincaré index for the nodes of the triangulation by considering vectors and triangles of the node's oriented star. The star of a node consists of all triangles with the node being

one of the triangle's vertices, ordered in counter-clockwise orientation w.r.t. the triangle normals. The angle of adjacent tangent vectors are measured in tangent space, i.e., triangles and vectors are first transformed in common flat space by unfolding the triangles along their common edge. For computing the Poincaré index in curved surface domains, the Gaussian curvature of the geometry needs to be considered. The Poincaré index is then

$$\text{idx}(c, \mathbf{v}) = \frac{\sum_{i=0}^{K-1} \angle(\mathbf{v}_i, \mathbf{v}_{(i+1)\%K})}{\sum_{i=0}^{K-1} \theta_i}, \quad (7)$$

for a node with an oriented star of K triangles with incident angles θ_i and tangent vectors v_i . The index is integer valued and denotes the number of oriented windings of the vectors around the center. Technically, the index is rounded to the nearest integer to account for floating point issues.

Continuous Fields. The discrete formula is correct as well if vectors are interpolated linearly along the edges of the grid. This holds especially for triangular grids and bilinear rectangular grids, the most common cases. For tangent vectors in 2D flat space given on the nodes of a grid, the denominator of Eq. (7) is 2π , the index is computed for the 2-cells; vectors of the nodes are traversed in counter-clockwise order.

Classification. The sign of the Poincaré index in 2D allows to discriminate between source/sink/center types of critical points (index > 0) and saddle type critical points (index < 0). To further distinguish between sources and sinks, we compute the divergence of the vector field. According to Gauss' theorem the total divergence of a volume element can be computed by considering the flux through a closed surface. For piecewise constant tangent vector fields, Polthier and Preuß [PP02] defined the divergence operator for a vertex c by

$$\text{div}(c, \mathbf{v}) = \frac{1}{2} \int_{\partial\text{star}(c)} \langle \mathbf{v}_i, \mathbf{n}_i \rangle, \quad (8)$$

the sum over the triangles of c 's star, and \mathbf{n}_i the exterior normal for each triangle along the star. For interpolated 2D fields, the divergence is computed as the sum of fluxes through the edges. The indicator functions are then

$$I_{\text{source}}(c, \mathbf{v}) = \begin{cases} 1 & \text{idx}(c, \mathbf{v}) > 0 \wedge \text{div}(c, \mathbf{v}) > 0 \\ 0 & \text{otherwise} \end{cases} \quad (9)$$

$$I_{\text{sink}}(c, \mathbf{v}) = \begin{cases} 1 & \text{idx}(c, \mathbf{v}) > 0 \wedge \text{div}(c, \mathbf{v}) < 0 \\ 0 & \text{otherwise} \end{cases} \quad (10)$$

$$I_{\text{saddle}}(c, \mathbf{v}) = \begin{cases} 1 & \text{idx}(c, \mathbf{v}) < 0 \\ 0 & \text{otherwise} \end{cases}. \quad (11)$$

Center type critical points with index 0 and divergence = 0 are not handled here. When dealing with numerical data, a divergence of exactly 0 does practically not occur. In the case of incompressible fluids that are known to be divergence-free center identification is performed by $I_{\text{center}} = I_{\text{source}} + I_{\text{sink}}$.

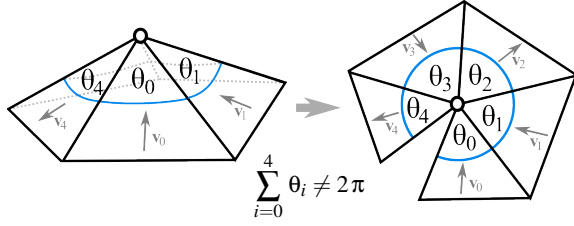


Figure 3: Star of a curved surface, incident angles around the center sum to less than 2π . Vector angles are measured in flattened space.

4.1.2. Critical Points in 3D

Analogously to the 2D case, the Poincaré index in 3D is given by the sum of oriented solid angles of the vectors of the volume's faces [GTS04]. For triangular faces of a tetrahedron with linearly interpolated vectors defined on the tetrahedron nodes, the vectors of a face span a spherical triangle with solid angle in $[-2\pi, 2\pi]$. The solid angles of all 4 faces divided by 4π is the Poincaré index in $\{-1, 0, +1\}$. Index -1 identifies sinks and saddles with an one dimensional stable manifold, index $+1$ identifies sources and saddles with an one dimensional unstable manifold. This leads to the indicator functions

$$I_+(c, \mathbf{v}) = \begin{cases} 1 & \text{idx}(c, \mathbf{v}) > 0 \\ 0 & \text{otherwise} \end{cases} \quad (12)$$

$$I_-(c, \mathbf{v}) = \begin{cases} 1 & \text{idx}(c, \mathbf{v}) < 0 \\ 0 & \text{otherwise} \end{cases}. \quad (13)$$

4.2. Swirling Motion

Swirling motion core-lines in 3D vector fields, as defined by Sujudi and Haimes [SH95], are lines where (i) the Jacobian J of the vector field has 2 complex eigenvalues, and (ii) the real eigenvector is parallel to the vectors along the lines. In a tetrahedral grid with vectors given on the grid nodes, the Jacobian is constant and vectors interpolate linearly within each tetrahedron. Thus, swirling motion cores are straight lines within a tetrahedron. We thus define our swirling motion feature indicator I_{swirl} on the vectors of a tetrahedron by 1 if a swirling motion core passes through the tetrahedron and 0 otherwise.

5. Parameter Estimation

We compute the probabilities of Eq. (4) with Monte Carlo sampling. We implemented the method for different grid-types and neighborhoods. To keep the implementation as independent as possible from grid topology, we implemented a value-gathering operation, that collects the cell's neighborhood data for each cell. For ensemble data with L members $\tilde{\mathbf{v}}_i \in \mathbb{R}^{K \times N}$ the vector valued sample mean

$$\hat{\mu} = \frac{1}{L} \sum_{i=1}^L \tilde{\mathbf{v}}_i \quad (14)$$

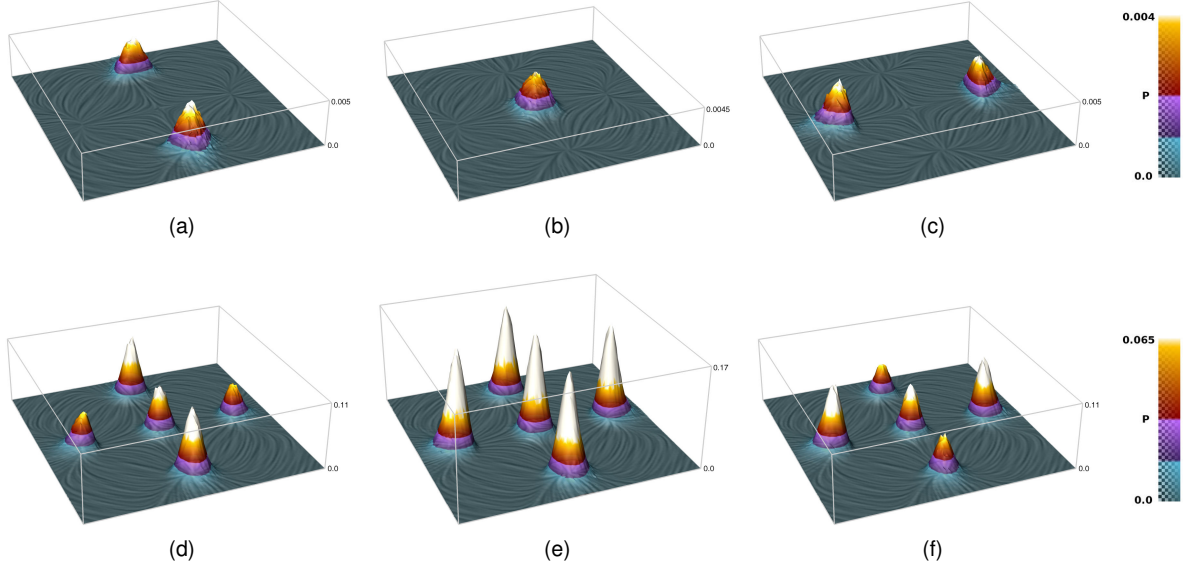


Figure 4: Synthetic dataset. From left to right: sources, saddles and sinks; top: correlation considered, bottom: correlation neglected. Note that the ranges of probabilities differ between the correlated and uncorrelated case and have been scaled for visualization. LIC visualizations display the mean field μ .

and sample covariance matrix

$$\hat{\Sigma} = \frac{1}{L-1} \sum_{i=1}^L (\tilde{\mathbf{v}}_i - \hat{\mu})(\tilde{\mathbf{v}}_i - \hat{\mu})^T \quad (15)$$

is computed directly on the gathered data. For the generation of multivariate normal distributed random numbers, a factorization $\hat{\Sigma} = A^T A$ is needed. If the matrix is positive definite, a Cholesky decomposition is applied. If it is just positive semi-definite, the more expensive spectral decomposition is used. Multi-variate normally distributed random values are computed using the Box-Muller method and transformed using the decomposed covariance matrix and $\hat{\mu}$ for Monte Carlo integration [Gen04]. Thus, main parts of the algorithm are independent of the grid topology. Only the value-gathering step and the indicator functions depend on it.

6. Visual Mapping

We employ two different methods to display the probabilities computed in 2D domains. The first method uses a heatmap with an additional colormapping. The second method uses an additive blending of distinct colors for source, sink and saddle probabilities. The first method is superior for flat domains, especially if they contain overlapping spatial distributions. The second method makes it possible to depict multiple probability fields simultaneously in a single visualization, and works well for fields with peaked and rather sparse spatial distributions. For 3D data we show colored nested transparent isosurfaces of the probability fields that indicate the spatial distribution of the respective features. To provide context and give a basic impression of the

uncertain vector field's trends we display LIC visualizations of the mean field μ in 2D fields and streamlines for 3D fields, respectively.

7. Results

We applied the probabilistic feature extraction methods to datasets from climate simulations and biofluid mechanics. Additionally, to illustrate basic properties of the methods and show the impact of spatial correlation, we present a synthetic example.

7.1. Synthetic Dataset

First, we applied our method to a dataset based on the formula proposed by Otto *et al.* [OGHT10]. With

$$v_c(x, y) = \begin{pmatrix} -x(1-x)(1+x)(1-y^2) - xy^2 \\ y(1-y)(1+y)(1-x^2) + yx^2 \end{pmatrix}, \quad (16)$$

we created an ensemble dataset with $L = 32$ members and $r = 0.2$ by

$$v_i(x, y) = v_c(x + r \cos \phi_i, y + r \sin \phi_i), \quad (17)$$

with $i \in \{1, \dots, L\}$, $\phi_i = \frac{2\pi i}{L}$, sampled on rectangular grids in $[-1, 1]^2$ with 128^2 samples. We computed the sample mean and sample covariance from this ensemble. In Fig. 4 (a),(b) and (c) the resulting probabilities are presented. Probabilities for the singularities are very close to the singularity distribution of the ensemble dataset. For the results in (d),(e) and (f) the correlations were neglected (the non-diagonal covariances are set to zero). Consequences of that are misclassifications of critical points and overestimation of probabilities.

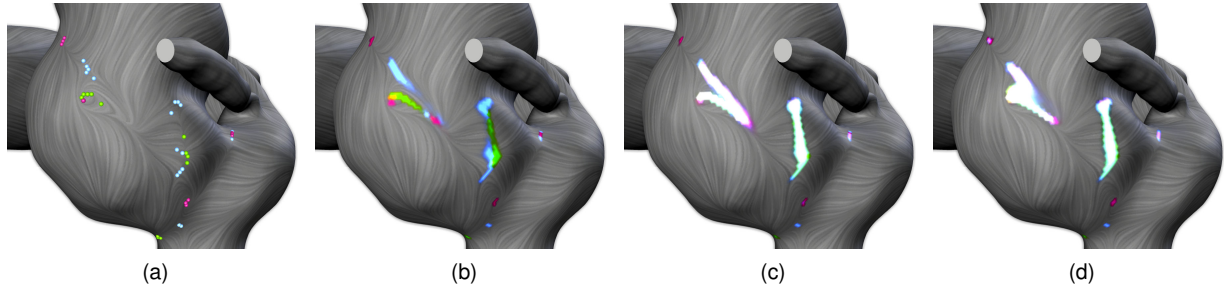


Figure 5: Color coded probabilities for singularities in the wall shear stress vector field from a simulated cerebral aneurysm blood flow at a single simulation time step. The mean wall shear stress vector field μ is indicated by a low-contrast LIC visualization. Probabilities for the different critical point types are encoded by different colors: sinks in violet, sources in green and saddles in blue. Intensities are scaled by the probabilities. Colors are blended additively. Depicted are: All critical points of the 9 ensemble members (a), probabilities considering spatial correlations (b), probabilities with correlations of vector components only (c) and probabilities with correlations neglected (d).

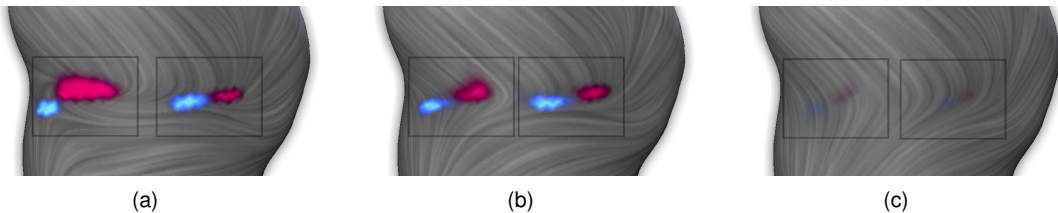


Figure 6: Critical point probabilities of the aneurysm wall-shear stress vector field at three subsequent time steps.

The expected values for the total number of critical points (equal to the sum of cell-wise probabilities) in the whole domain are:

correlation	$E(\#\text{source})$	$E(\#\text{saddle})$	$E(\#\text{sink})$
considered	1.9	1.0	1.9
neglected	57.3	111.6	57.4

Thus, by considering spatial correlations these numbers reproduce very closely the numbers of critical points in every ensemble member. Probabilities are significantly overestimated in the uncorrelated case.

7.2. Aneurysm Dataset

We inspected uncertain features of the wall-shear stress vector field and the blood flow velocity field in a cerebral aneurysm, resulting from time-dependent biofluid mechanical simulations. Aneurysm geometry was reconstructed from an individual patient. Modelling parameters are affected by uncertainty: patient-specific flow-rates could not be measured in clinical practice and are taken from a textbook; the hematocrit value of the blood changes over time. To inspect the impact of these uncertainties on the positions of flow singularities, we studied an uncertain vector field defined by an ensemble of simulation results obtained with 9 different parameter configurations. From the ensemble we estimated the sample mean vectors $\hat{\mu}$ and sample covariance matrices $\hat{\Sigma}$.

Fig. 5 depicts probabilities for source, sink and saddle type critical points at a single time step of the simulation. Fig. 5 (a) depicts the critical points of all 9 ensemble members by colored spheres. The points are computed for the nodes of the triangulated surface, multiple occurrences of critical points at the same nodes are possible. Critical points of different ensemble members are close-by. In (b), critical point probabilities of the uncertain vector field with $\hat{\mu}$ and $\hat{\Sigma}$ are depicted. The similarity to (a) is high but non-vanishing probabilities also occur in other areas of low vector magnitude where the amount of uncertainty exceeds the mean. We studied the influence of the covariances by assuming statistical independence of the vectors among one another in (c), and of all components of the random vector in (d), i.e., by dropping all the covariances. In both cases, the distinctive power for the type of critical point diminishes, indicated by the white color, resulting from an additive blending of colors associated to high probabilities for all critical point types.

Three subsequent time steps at $t = 0.57s$, $0.61s$ and $0.63s$ at a heart cycle of $1s$ are displayed in Fig. 6. During time, the probabilities for critical points of sinks and saddles disappear pair-wise. The following table lists the expected values for the number of saddles and sinks on the left (E_l) and right (E_r), for the time steps of Fig. 6. The areas over which the expectations were computed are indicated by rectangles.

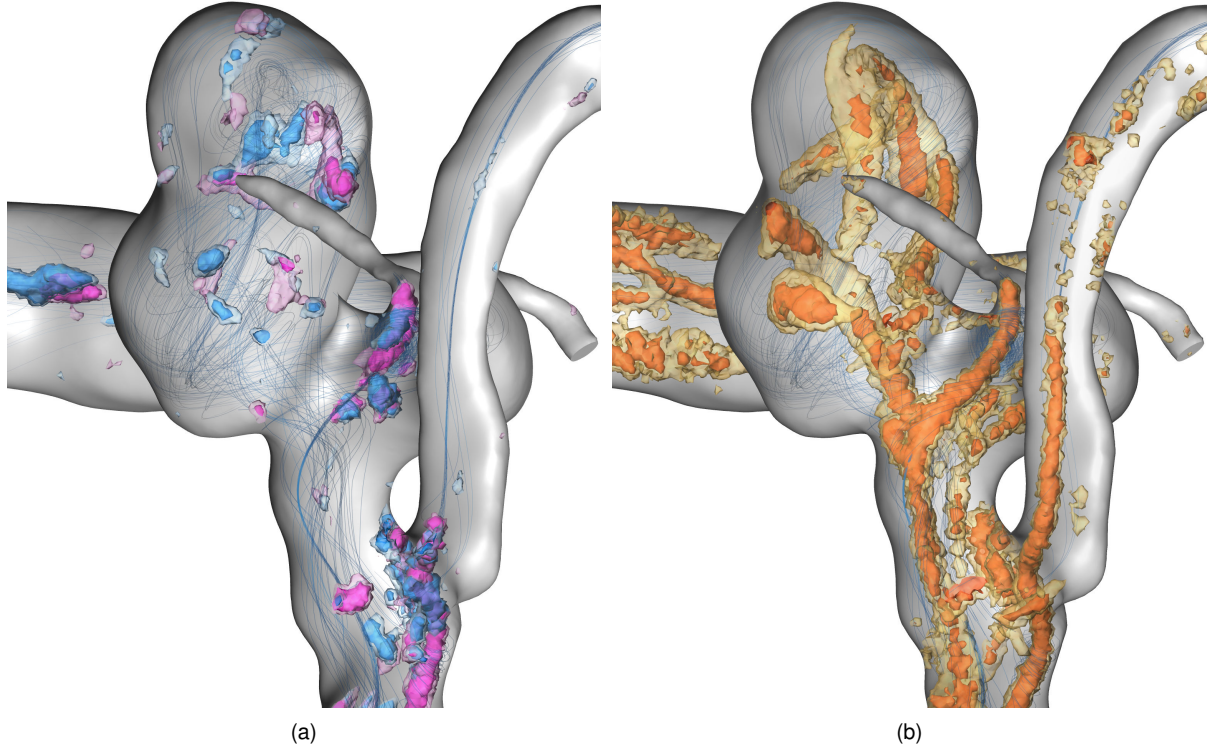


Figure 7: Uncertain flow features over a full heart cycle in a cerebral aneurysm visualized by nested semi-transparent isosurfaces. Streamlines of the mean vector field reveals some context. (a) Critical point probabilities with Poincaré index > 0 (blue) and < 0 (violet). (b) Probabilities for swirling motion cores.

t/s	$E_l(\#saddles)$	$E_l(\#sinks)$	$E_r(\#saddles)$	$E_r(\#sinks)$
0.57	0.99	0.99	0.26	0.26
0.61	0.23	0.22	0.2	0.19
0.63	0.03	0.03	0.01	0.01

The temporal evolution of the uncertain critical points can be observed in the movie provided as supplementary material.

Results in 3D are presented in Fig. 7. We computed means and covariances for a single parameter setting, but for all time-steps of a heart cycle simulation. In (a) the critical points are depicted. As blood is an incompressible fluid, all critical points are of saddle-type. Critical point probabilities are more focused at vessel bifurcations and more fuzzy in the dome region of the aneurysm. Critical point type distinction with Poincaré index > 0 (1D unstable manifold) and < 0 (1D stable manifold) is observable as well. Probabilities for Sujudi-Haines swirling motion cores are depicted in (b). The time-variation of vortical structures is higher in the dome-region of the aneurysm in comparison to the vortical flow in the vessels.

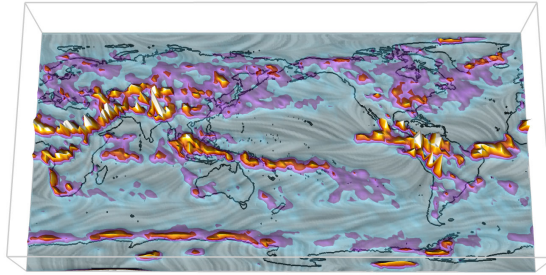
7.3. Climate Simulation Data

We analyzed ensemble datasets from the DEMETER project [Pal04] to obtain distributions for singularities in the 10-

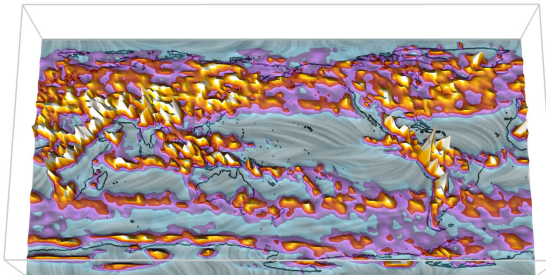
meter-wind velocity vector fields. For each timestep, 63 realizations of daily average wind velocities constitute an ensemble, where the results are generated by 7 different climate models and 9 different sets of simulation parameters. From these results we compute the means μ and covariances Σ for each grid cell of the rectilinear 2D grid.

In Fig. 8 the probabilities for singularities in the uncertain 10-meter wind vector field are shown as a heightfield with colormapping. The mean vector field μ is indicated as a LIC visualization below the heightfield. In Fig. 8 (a) the probabilities for the existence of sources, (b) saddles and (c) for sinks are shown. Source- and sink probabilities are mainly high over the landmass, especially mountains attract this behavior. This is reasonable, as source and sink behavior in a 2D slice denote lifting and falling wind. An overview of saddle probabilities for all time steps is included in the movie in the supplementary material.

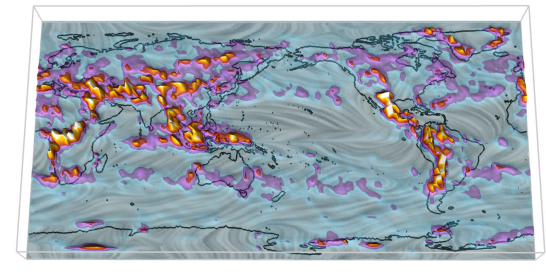
Fig. 9 shows the influence of spatial covariances. Displayed are cut-outs of sink probabilities in Middle America. In (a), spatial covariances are considered, in (b) only vector-wise covariances are considered, and in (c) no covariances are considered. Including spatial covariances drastically reduces the probabilities; the influence of the vector-wise covariances of (b) is practically not distinguishable from (c).



(a)



(b)

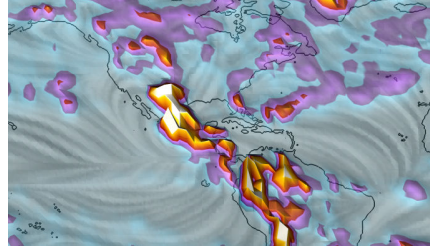
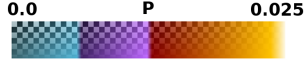


(c)

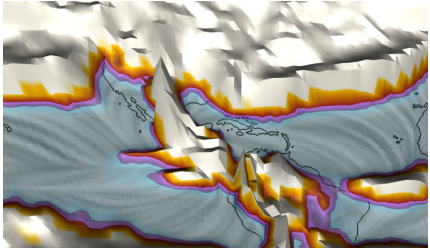
Figure 8: Probabilities for singularities in the daily average wind vector field from the climate simulation dataset are shown as a heightfield with colormapping. (a) sources, (b) saddles, (c) sinks.

8. Discussion

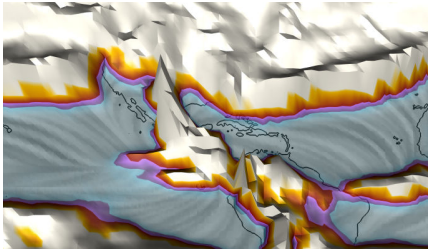
The results show that our approach for the computation of probability fields for local features considering local covariance structures works very well in practice. As depicted in Fig. 5 (a) and (b), singularities in the aneurysm wall-shear stress vector field of the ensemble members agree very well with the computed probability fields. Ensemble critical points are clustered, the probability fields are localized as well. Following critical point probability fields over time as done in Fig. 6 confirms the fact of crisp singularities that critical points with index +1 and -1 appear or disappear pairwise. Probabilities for sinks and saddles fade out simultaneously with roughly the same amount. Recent studies have shown that low wall-shear stress in the dome region is connected to increased rupture risk of certain cere-



(a)



(b)



(c)

Figure 9: Cutout of the probability fields for sinks: (a) With correlations, (b) just vector-wise correlations, (c) without consideration of correlations.

bral aneurysms [GSK^{*}12]. The time evolution of probabilities of critical points, particularly their spatial stability and variability, as shown in the supplementary movie, provides information that domain experts considered as important.

Our method allows to distinguish between different critical point types. This classification proved to produce meaningful results. The spatial covariances capture spatial derivatives very well. In the synthetic dataset of Fig. 4, practically no overlapping classifications are found. In the wall shear stress field of the aneurysm dataset, regions with high overlapping probabilities for different critical point types are rare and differentiation is precise, even if the different critical point probabilities are very close-by. Some more overlap is observable in 3D, but the different regions are still fairly separated. Singularities in the climate wind velocity dataset are

much less separated. Notable differences between source, saddle and sink probabilities are also observable in Fig. 8.

We applied the Sujudi and Haimes swirling motion vortex core criterion on piecewise linear vector fields without filtering or strength assessment. In a crisp vector field, this leads to discontinuous line segments with a lot of clutter due to weak swirling behavior. Nevertheless, the resulting probabilities in the aneurysm dataset in Fig. 7 correspond very much to the main vortices. This is due to an implicit smoothing effect in the uncertainty setting, where weak features are spatially less concentrated and have lower probabilities. The chosen vortex criterion is more direct, compared to other methods using vortex indicating scalar fields, like e.g. λ_2 [JKJTM06]. The scalar fields would require additional processing steps (thresholding or ridge extraction) to yield Boolean feature detectors. Pointwise statistical analysis of physical quantities over heart cycles is common practice in the application domain, see e.g. [BRM*08, GSK*12], though, a Gaussian model might be a too rough approximation for the velocities of the pumping flow. Thus, further analyses of the input data are necessary, and possibly an extended statistical framework needs to be developed.

Neglecting spatial covariances has two notable effects. First, the ability to distinguish between critical point types is reduced, and second, probabilities are significantly overestimated. The reason for this is that neglecting correlation corresponds to a white-noise-model for the uncertainty. Disturbance of vector fields by white noise leads to a much larger number of critical points and thus higher cell-wise probabilities. Spatial covariances between adjacent samples are more important, the differences between fully uncorrelated random variables and vector-wise correlated random variables are not that large. Localized high probability areas for critical points do not necessarily have counterparts in the mean vector field, as can be observed in Fig. 6 (b) and (c). It is therefore not sufficient to annotate features of the mean field with probabilities.

The proposed feature indicators are defined on the smallest possible scales represented by the sampling grid. The interpretation of the results must account for this. In case features on larger scales are of interest, indicator function domain sizes would need to be adjusted accordingly.

Running times for the computation of the probability fields are quite high, due to the Monte Carlo integration. For each data set, the number of samples was chosen manually, such that no Monte Carlo noise was observable anymore. Computation of the probabilities for the aneurysm wall shear stress features for a single time step takes several minutes, computation of volume features in the aneurysm flow requires several hours with non-optimized code on a state-of-the art 8-core machine. An advantage of our local approach is that only local covariances are needed and thus the memory requirements are not quadratic in the number of cells as it would be if the complete correlation structure was stored.

Our method for critical point detection is closely related to the method proposed by Otto *et al.* [OGHT10, OGT11b, OGT11a]. Both methods compute scalar fields to indicate relative critical point strengths. We compute cell-wise probabilities, Otto *et al.* density fields that are normalized to an integral of 1. The approaches differ significantly. We consider critical points as local features, whereas Otto *et al.* consider them as global features. Thus, results are not directly comparable. Saddle detection ability is intrinsic in the local approach, more algorithmic effort (computation of the gradient of the squared velocity of the uncertain vector field) is needed in the global approach. The global approach seems to be insensitive to neglecting correlations; this deserves further research. The implementation complexity differs; we think that our local method is conceptually easier and easier to implement.

Our approach is limited to local features. Similar to crisp vector field analysis, features that are global by nature such as (closed) streamlines or separatrices are detectable with global methods only.

9. Conclusions and Future Work

We presented a general framework for the extraction of probabilistic local features from uncertain vector fields under consideration of the spatial correlation structure. We defined probabilistic equivalents to critical points in uncertain 2D and 3D vector fields and cores of swirling motion in 3D. Our results computed from biofluid mechanics and climate research data indicate significant differences in the spatial locality of features and show that the consideration of correlation is essential for obtaining correct results.

In contrast to previous global methods [OGHT10, OGT11a, OGT11b], we take a different perspective on the topic. Our local method is able to extract features also in divergence-free fields and to detect saddle points in a straightforward way. It works on different grid types including surface vector fields.

The big impact of correlations observed with the local method raises the question whether the results of global methods, if extended to consider correlations, would also be affected significantly. This deserves further research. Another area of research will be the evaluation of improvements or alternatives to the Monte Carlo method (e.g. quasi-Monte Carlo techniques, automated check of convergence) in order to reduce computation times.

Acknowledgements

We are grateful to Leonid Goubergrits and Jens Schaller for helpful discussions and the provision of aneurysm datasets. We also thank the ECMWF [Pal04] for the climate dataset. This work was supported by the German Research Foundation (DFG HE 2948/5-3).

References

- [AOB09] ALLENDES OSORIO R. S., BRODLIE K. W.: Uncertain Flow Visualization using LIC. In *7th EG UK Theory and Practice of Computer Graphics: Proceedings. 7th Theory and Practice of Computer Graphics* (2009), Tang W., Collomosse J., (Eds.), Eurographics Association Eurographics UK Chapter. [2](#)
- [BJB*11] BHATIA H., JADHAV S., BREMER P.-T., CHEN G., LEVINE J. A., NONATO L. G., PASCUCCI V.: Flow visualization with quantified spatial and temporal errors using edge maps. *IEEE Trans. Vis. Comput. Graph.*, PrePrints (2011). [2](#)
- [BRM*08] BOUSSEL L., RAYZ V., MCCULLOCH C., MARTIN A., ACEVEDO-BOLTON G., LAWTON M., HIGASHIDA R., SMITH W. S., YOUNG W. L., SALONER D.: Aneurysm growth occurs at region of low wall shear stress: patient-specific correlation of hemodynamics and growth in a longitudinal study. *Stroke* 39, 11 (2008), 2997–3002. [9](#)
- [BWE05] BOTCHEN R. P., WEISKOPF D., ERTL T.: Texture-based visualization of uncertainty in flow fields. In *Proceedings of IEEE Visualization 2005* (2005), IEEE, pp. 647–654. [2](#)
- [FHH*10] FRIMAN O., HENNEMUTH A., HARLOFF A., BOCK J., MARKL M., PEITGEN H.: Probabilistic 4d blood flow mapping. *Medical Image Computing and Computer-Assisted Intervention–MICCAI 2010* (2010), 416–423. [2](#)
- [FLS63] FEYNMAN R. P., LEIGHTON R. B., SANDS M.: *The Feynman Lectures on Physics*, vol. 1. Caltech, Caltech, 1963, ch. 6 Probability, p. 10. [1](#)
- [Gen04] GENTLE J. E.: *Random Number Generation and Monte Carlo Methods*, 2nd ed. Springer, 2004. [5](#)
- [GSK*12] GOUBERGRITS L., SCHALLER J., KERTZSCHER U., VAN DEN BRUCK N., PÖTHKOW K., PETZ C., HEGE H.-C., SPULER A.: Statistical wall shear stress maps of ruptured and unruptured middle cerebral artery aneurysms. *J. R. Soc. Interface* 9, 69 (2012), 677 – 688. [8, 9](#)
- [GTS04] GARTH C., TRICOCHE X., SCHEUERMANN G.: Tracking of vector field singularities in unstructured 3d time-dependent datasets. In *Proc. IEEE Vis. 2004* (2004), pp. 329–336. [2, 4](#)
- [H89] HELMAN J. L., HESSELINK L.: Representation and display of vector field topology in fluid flow data sets. *Computer* 22 (August 1989), 27–36. [2](#)
- [HLNW11] HLAWATSCH M., LEUBE P., NOWAK W., WEISKOPF D.: Flow radar glyphs - static visualization of unsteady flow with uncertainty. *IEEE Trans. Vis. Comput. Graph.* 17, 12 (2011), 1949–1958. [2](#)
- [JKJTM06] JANKUN-KELLY M., JIANG M., THOMPSON D., MACHIRAJU R.: Vortex visualization for practical engineering applications. *IEEE Trans. Vis. Comput. Graph.* 12, 5 (2006), 957–964. [9](#)
- [JS03] JOHNSON C. R., SANDERSON A. R.: A next step: Visualizing errors and uncertainty. *IEEE Computer Graphics and Applications* 23, 5 (2003), 6–10. [2](#)
- [LFC02] LODHA S. K., FAALAND N. M., CHARANIYA A. P.: Visualization of uncertain particle movement. In *Proceedings of the Computer Graphics and Imaging Conference* (2002), pp. 226–232. [2](#)
- [LHZP07] LARAMEE R., HAUSER H., ZHAO L., POST F.: Topology-based flow visualization, the state of the art. *Topology-based Methods in Visualization* (2007), 1–19. [2](#)
- [LPSW96] LODHA S. K., PANG A., SHEEHAN R. E., WITTENBRINK C. M.: Uflow: visualizing uncertainty in fluid flow. In *Proceedings IEEE Visualization 1996* (1996), pp. 249–254. [2](#)
- [MLP*10] MCLOUGHLIN T., LARAMEE R., PEIKERT R., POST F., CHEN M.: Over two decades of integration-based, geometric flow visualization. In *Computer Graphics Forum* (2010), vol. 29:6, pp. 1807–1829. [2](#)
- [OGHT10] OTTO M., GERMER T., HEGE H.-C., THEISEL H.: Uncertain 2D vector field topology. *Comput. Graph. Forum* 29 (2010), 347–356. [2, 5, 9](#)
- [OGT11a] OTTO M., GERMER T., THEISEL H.: Closed stream lines in uncertain vector fields. In *Proc. Spring Conference on Computer Graphics (SCCG)* (2011). [2, 9](#)
- [OGT11b] OTTO M., GERMER T., THEISEL H.: Uncertain topology of 3d vector fields. In *Proceedings of 4th IEEE Pacific Visualization Symposium (PacificVis 2011)* (Hong Kong, China, March 2011), pp. 67–74. [2, 9](#)
- [Pal04] PALMER, T. N. ET AL.: Development of a European multi-model ensemble system for seasonal to inter-annual prediction (DEMIETER). *Bulletin of the American Meteorological Society* 85, 6 (2004), 853–872. [7, 9](#)
- [PH11] PÖTHKOW K., HEGE H.-C.: Positional uncertainty of isocontours: Condition analysis and probabilistic measures. *IEEE Trans. Vis. Comput. Graph.* 17, 10 (2011), 1393–1406. [2](#)
- [PP02] POLTHIER K., PREUSS E.: Identifying vector field singularities using a discrete hodge decomposition. In *Visualization and Mathematics III* (2002), Springer, pp. 112–134. [2, 4](#)
- [PRW11] PFAFFELMOSER T., REITINGER M., WESTERMANN R.: Visualizing the positional and geometrical variability of isosurfaces in uncertain scalar fields. *Computer Graphics Forum* 30, 3 (2011), 951–960. [1, 2](#)
- [PVH*03] POST F., VROLIJK B., HAUSER H., LARAMEE R., DOLEISCH H.: The state of the art in flow visualisation: Feature extraction and tracking. In *Computer Graphics Forum* (2003), vol. 22:4, pp. 775–792. [2](#)
- [PWH11] PÖTHKOW K., WEBER B., HEGE H.-C.: Probabilistic marching cubes. *Computer Graphics Forum* 30, 3 (2011), 931 – 940. [1, 2, 3](#)
- [PWL97] PANG A. T., WITTENBRINK C. M., LODHA S. K.: Approaches to uncertainty visualization. *The Visual Computer* 13, 8 (1997), 370–390. [2](#)
- [SH95] SUJUDI D., HAIMES R.: *Identification of swirling flow in 3D vector fields*. Tech. rep., Dept. of Aeronautics and Astronautics, MIT, Cambridge, MA, 1995. [2, 4](#)
- [SJK04] SANDERSON A. R., JOHNSON C. R., KIRBY R. M.: Display of vector fields using a reaction-diffusion model. In *Proceedings of IEEE Visualization 2004* (2004), pp. 115–122. [2](#)
- [Szy11] SZYMCZAK A.: Stable morse decompositions for piecewise constant vector fields on surfaces. *Computer Graphics Forum* 30, 3 (2011), 851–860. [2](#)
- [TG09] TRICOCHE X., GARTH C.: Topological methods for visualizing vortical flows. In *Mathematical Foundations of Scientific Visualization, Computer Graphics, and Massive Data Exploration*, Farin G., Hege H.-C., Hoffman D., Johnson C. R., Polthier K., (Eds.), Mathematics and Visualization. Springer, 2009, pp. 89–107. [2](#)
- [WPL96] WITTENBRINK C. M., PANG A. T., LODHA S. K.: Glyphs for visualizing uncertainty in vector fields. *IEEE Trans. Vis. Comput. Graph.* 2, 3 (1996), 266–279. [2](#)
- [ZDG*08] ZUK T., DOWNTON J., GRAY D., CARPENDALE S., LIANG J.: Exploration of uncertainty in bidirectional vector fields. In *Proc. SPIE & IS&T Conf. Electronic Imaging, Vol. 6809: Visualization and Data Analysis 2008* (2008), vol. 6809, SPIE, p. 68090B. [2](#)